

Effects of radiative interior on solar inertial modes

Suprabha Mukhopadhyay¹, Yuto Bekki¹, Xiaoqie Zhu¹, and Laurent Gizon^{1,2}

¹ Max-Planck-Institut für Sonnensystemforschung, Justus-von-Liebig-Weg 3, 37077 Göttingen, Germany

² Institut für Astrophysik und Geophysik, Georg-August-Universität Göttingen, Friedrich-Hund-Platz 1, 37077 Göttingen, Germany
e-mail: gizon@mps.mpg.de, e-mail: zhux@mps.mpg.de

Received / accepted

ABSTRACT

Context. The solar inertial modes are expected to play important diagnostic and dynamical roles in the Sun’s differentially rotating convection zone. The coupling of these modes to the radiative interior is yet to be discussed.

Aims. We aim to understand the dependence of the modes on the uniformly rotating subadiabatic region below the convection zone, and whether this leads to measurable changes at the surface.

Methods. We used the *Dedalus* code to compute the linear eigenmodes in the inertial frequency range in a setup including both the convection zone and the radiative interior down to $0.5R_\odot$. We imposed free-surface boundary conditions at both radial boundaries. For comparison, we also computed the eigenmodes in a setup restricted to the convection zone.

Results. We find that the inclusion of the radiative zone only slightly modifies the frequencies and the eigenfunctions at the surface, excluding some modes with significant radial motions (high-frequency retrograde and prograde columnar modes). On the other hand, most modes penetrate significantly into the overshooting layer below the convection zone, which significantly reduces the growth rate of the modes and distorts their eigenfunctions near the base of the convection zone. Furthermore, the uniformly rotating subadiabatic radiative zone supports oscillations due to Rossby modes of all possible spherical harmonics and radial nodes. In particular, when the nearest inertial mode in frequency space lies within around 10 nHz and shares the same north–south symmetry, these Rossby modes evolve into mixed modes characterized by significant motions within both the radiative and convection zones. However, such mixed modes have a large mode mass in the radiative interior and thus will be difficult to excite stochastically by convection.

Key words. Sun: oscillations - Sun: interior - Sun: rotation - Hydrodynamics - Instabilities

1. Introduction

Inertial modes are global oscillations in a rotating fluid whose restoring force is the Coriolis force. Different classes of inertial modes have been identified in the solar near-surface flows using various observational datasets and techniques (see [Gizon et al. 2024](#), for a review). These include the equatorial Rossby modes ([Löptien et al. 2018](#)), critical-latitude and high-latitude modes ([Gizon et al. 2021](#)), and the so-called high-frequency retrograde (HFR) modes ([Hanson et al. 2022](#)). All observed modes propagate retrograde with respect to the fastest local rotation rate, i.e. the surface equatorial rotation rate (or the Carrington rotation rate). The solar inertial modes are found to be very sensitive to the solar differential rotation in the convection zone (Fig. 1a), as well as to several unknown quantities in the deep interior, such as turbulent viscosity and superadiabaticity (e.g. [Gizon et al. 2021](#); [Bekki et al. 2022b](#); [Fournier et al. 2022](#); [Hanson & Hanasoge 2024](#)). Diagnosing these physical quantities using inertial modes may improve our understanding of the global-scale flow dynamics. Apart from their diagnostic role, the solar inertial modes may also play a significant dynamical role by providing non-linear feedback to regulate the Sun’s differential rotation ([Bekki et al. 2024](#)).

Linear models in 2D and 3D have helped identify the inertial modes and understand their physics (e.g. [Gizon et al. 2020](#); [Bekki et al. 2022b](#); [Fournier et al. 2022](#); [Bhattacharya & Hanasoge 2023](#); [Mukhopadhyay et al. 2025](#)). So far, most theoretical studies of inertial modes have been done only in the convection zone with impenetrable boundary conditions in the radial

direction. It remains unclear how the radiative interior affects the properties of solar inertial modes in the convection envelope.

[Blume et al. \(2024\)](#) recently presented a non-linear simulation with the radiative interior and showed that both sectoral and tesseral Rossby modes are ubiquitously found in the radiative interior. It is implied that these toroidal Rossby modes are likely present in a wave cavity different from the one in the convection zone. [Matilsky et al. \(2022\)](#) further proposed that these Rossby modes might play a role in the confinement of the tachocline or in generating the local dynamo in the radiative zone. In the aforementioned studies, however, the spatial eigenfunctions of these Rossby modes were not reported, and the mode coupling between the radiative and convective zones is still not well understood.

The presence of a convectively stable stratification allows for the existence of (gravito-)inertial modes whose restoring forces are both buoyancy and Coriolis forces. Gravito-inertial modes are important for inferring rotation profiles in γ Doradus stars, which have convective cores and radiative envelopes (e.g. [Ouazzani et al. 2020](#); [Tokuno & Takata 2022](#)). These modes can be classified into two types: inertial modes modified by buoyancy and gravity modes modified by rotation (e.g. [Dintrans & Rieutord 2000](#)). In the Sun’s radiative interior, the Brunt–Väisälä frequency is about two orders of magnitude higher than the rotation rate. Thus, most attention has so far been focused on the perturbations of gravity modes by rotation (e.g. [Alvan et al. 2014](#)), rather than on inertial modes perturbed by gravity or buoyancy.

In this paper, we conduct a linear eigenmode analysis for the solar case, including not only quasi-toroidal inertial modes but

also non-toroidal inertial modes (HFR and columnar convective modes), and study how they behave when they couple to the radiative interior. Given the high precision and accuracy of solar inertial mode observations, accurate computations of both frequencies and eigenfunctions are essential for interpreting these observations. Coupling to the radiative zone (RZ) may potentially influence the eigenmodes restricted to the convection zone (CZ) shell alone. We also study Rossby modes in the radiative interior, which are perturbed by buoyancy due to the subadiabatic stratification. The paper is organized as follows. In Sect. 2, we describe our model of small-amplitude inertial modes covering both the CZ and the upper RZ. The eigenfunctions and spectra of the selected inertial modes computed in the setup are analysed in Sect. 3. Finally, we discuss the implications of our results in Sect. 4.

2. Inertial modes in a model combining CZ and RZ

We used the flexible spectral code *Dedalus* (Burns et al. 2020) to solve the linear eigenvalue problem for low-frequency modes of oscillation in the Sun. We employed the same approach as in Mukhopadhyay et al. (2025). The setup used in this paper encompasses the upper RZ and CZ of the Sun, with free-surface boundary conditions applied at the top and bottom of the domain. We used a fully compressible model as gravity modes in the radiative interior have been found to be affected by the anelastic approximation (e.g. Brown et al. 2012; Vasil et al. 2013; Hindman & Julien 2024).

2.1. Equations for linear oscillations

We solved for the linearized compressible fluid dynamical equations:

$$\frac{\partial \mathbf{u}}{\partial t} + \mathbf{v}_0 \cdot \nabla \mathbf{u} + \mathbf{u} \cdot \nabla \mathbf{v}_0 + 2\Omega_0 \mathbf{e}_z \times \mathbf{u} + \frac{\nabla p_1}{\rho_0} + \frac{\rho_1}{\rho_0} g \mathbf{e}_r - \frac{1}{\rho_0} \nabla \cdot (\nu \rho_0 \mathbf{S}) = 0, \quad (1)$$

$$\frac{\partial s_1}{\partial t} + \mathbf{v}_0 \cdot \nabla s_1 + u_r \frac{\partial s_0}{\partial r} + \frac{u_\theta}{r} \frac{\partial s_0}{\partial \theta} - \frac{1}{\rho_0 T_0} \nabla \cdot (\kappa \rho_0 T_0 \nabla s_1) = 0, \quad (2)$$

$$\frac{\partial \rho_1}{\partial t} + \nabla \cdot (\rho_0 \mathbf{u}) + \nabla \cdot (\rho_1 \mathbf{v}_0) = 0, \quad (3)$$

in combination with the linearized quasi-adiabatic equation of state (e.g. Unno et al. 1979)

$$\frac{p_1}{p_0} = \Gamma_1 \frac{\rho_1}{\rho_0} + \Gamma_1 \nabla_{\text{ad}} \frac{\rho_0 T_0}{p_0} s_1. \quad (4)$$

In the above equations, \mathbf{u} , ρ_1 , p_1 , and s_1 denote the perturbations of velocity, density, pressure, and entropy with respect to the background. We consider the background density ρ_0 , pressure p_0 , temperature T_0 , gravitational acceleration g , first adiabatic exponent Γ_1 , and adiabatic gradient ∇_{ad} from the standard solar Model S (Christensen-Dalsgaard et al. 1996). The equations were formulated in the Carrington frame of reference rotating at $\Omega_0/2\pi = 456$ nHz. In this frame, the base flow $\mathbf{v}_0 = (\Omega(r, \theta) - \Omega_0) r \sin \theta \mathbf{e}_\phi$ denotes the Sun's differential rotation. The background latitudinal entropy gradient ($\partial s_0 / \partial \theta$) is estimated under the assumption of thermal wind balance for solar differential rotation (e.g. Pedlosky 1982; Thompson et al. 2003). The remaining quantities in the model equations are described in the following subsections.

2.2. Differential rotation model

In most of our calculations, we used a simplified analytic profile for the differential rotation given by

$$\Omega(r, \theta) = \Omega_{\text{CZ}}(\theta) + \frac{(\Omega_{\text{RZ}} - \Omega_{\text{CZ}}(\theta))}{2} \left[1 + \text{erf} \left(\frac{r_{\text{tc}} - r}{d_{\text{tc}}} \right) \right], \quad (5)$$

where $r_{\text{tc}} = 0.71 R_\odot$ and $d_{\text{tc}} = 0.045 R_\odot$ are the position and thickness of the tachocline, respectively. We assumed that, the RZ rotates rigidly at $\Omega_{\text{RZ}}/2\pi = 433.5$ nHz, while the CZ has a rotational shear in latitude as

$$\Omega_{\text{CZ}}(\theta) = \Omega_1 + \Omega_2 \cos^2 \theta + \Omega_3 \cos^4 \theta, \quad (6)$$

with $\Omega_1/2\pi = 464$ nHz, $\Omega_2/2\pi = -76$ nHz, and $\Omega_3/2\pi = -50$ nHz. This simplified profile allowed separation of the radial and latitudinal dependencies and reduced memory usage in *Dedalus* solver, which enabled us to use a higher grid resolution to better resolve modes with many radial nodes.

However, only while modelling the high-latitude modes, we used the actual data of the Sun's differential rotation measured by helioseismology (from Larson & Schou 2018). This is because the baroclinically unstable high-latitude modes are known to sensitively depend on the profiles of differential rotation and the associated latitudinal entropy gradient (Gizon et al. 2021; Bekki et al. 2022a). The observed and simplified profiles of the differential rotation are compared in Fig. 1. The shaded regions in Fig. 1c are described in the following subsection.

2.3. Turbulent diffusivities and superadiabaticity

The strain-rate tensor is given by

$$\mathbf{S} = \nabla \mathbf{u} + \nabla \mathbf{u}^T - \frac{2}{3} (\nabla \cdot \mathbf{u}) \mathbf{I}_3. \quad (7)$$

We used radially varying profiles of turbulent viscosity ν and turbulent thermal diffusivity κ , similar to Nandy & Choudhuri (2002), given by

$$\nu(r) = \nu_{\text{RZ}} + \frac{(\nu_{\text{CZ}} - \nu_{\text{RZ}})}{2} \left[1 + \text{erf} \left(\frac{r - r_{\text{OS}}}{d_{\text{OS}}} \right) \right], \quad (8)$$

$$\kappa(r) = \kappa_{\text{RZ}} + \frac{(\kappa_{\text{CZ}} - \kappa_{\text{RZ}})}{2} \left[1 + \text{erf} \left(\frac{r - r_{\text{OS}}}{d_{\text{OS}}} \right) \right]. \quad (9)$$

Here, the turbulent viscosity and thermal diffusivity in the CZ (ν_{CZ} , κ_{CZ}) were both set to be 10^{12} cm² s⁻¹. In the RZ below, we adopted the values $\nu_{\text{RZ}} = 10^{10}$ cm² s⁻¹ and $\kappa_{\text{RZ}} = 4 \times 10^{10}$ cm² s⁻¹. We assumed a slightly higher value of thermal diffusivity than turbulent viscosity in the RZ to account for the effects of radiation (e.g. Brun et al. 2011; Brown et al. 2012). We used the parameters for the transition depth $r_{\text{OS}} = 0.7 R_\odot$ and the transition thickness $d_{\text{OS}} = 0.04 R_\odot$. The left panel of Fig. 2 shows the radial profiles of ν and κ used in this study.

The background radial entropy gradient, $\partial s_0 / \partial r$, denotes the degree of convective instability in the background stratification. Although the RZ is strongly subadiabatic (convectively stable), uncertainty remains regarding superadiabaticity in the bulk CZ. While the model S predicts a superadiabatic stratification within the whole CZ, it has been questioned by recent observations and numerical models of solar large-scale convection (e.g. Käpylä et al. 2017; Gizon et al. 2021; Hotta et al. 2022; Bekki 2024). In this study, we employed the following step function for $\partial s_0 / \partial r$,

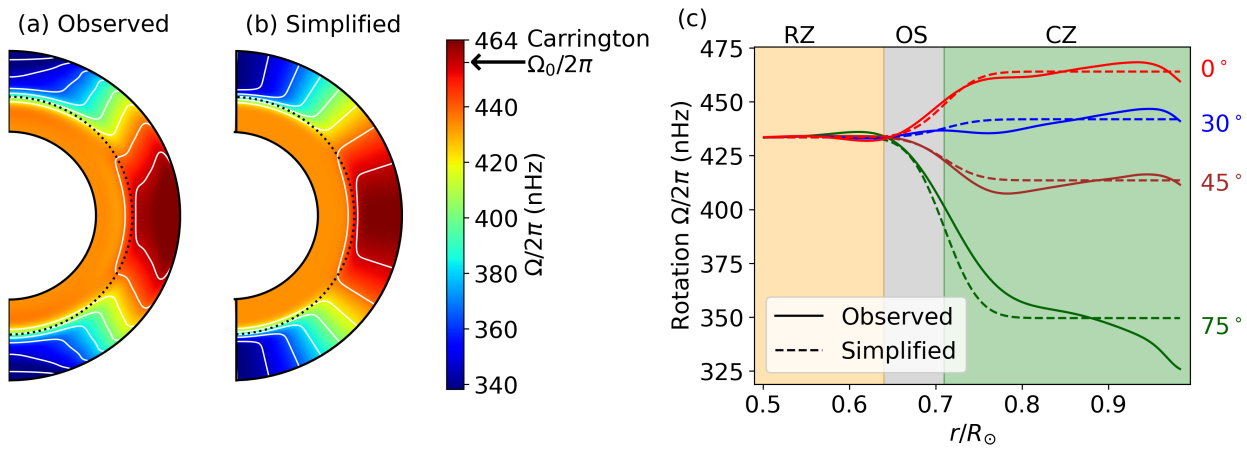


Fig. 1. Profiles of differential rotation used in this study. (a) The observed two-dimensional profiles in a meridional plane, taken from Larson & Schou (2018) (b) The simplified differential rotation profile, given by Eq. (5), to model the observed differential rotation. The dotted black lines indicate the base of the convection zone at $r = 0.71R_\odot$. The Carrington rotation rate $\Omega_0/2\pi = 456$ nHz is marked on the colour-bar. (c) Cuts of observed (solid) and simplified (dashed) differential rotation profiles at fixed latitudes; 0° (red), 30° (blue), 45° (brown), and 75° (dark green). The green shaded area denotes the convection zone, the grey shaded region denotes the overshooting layer, and the orange shaded region denotes the radiative zone.

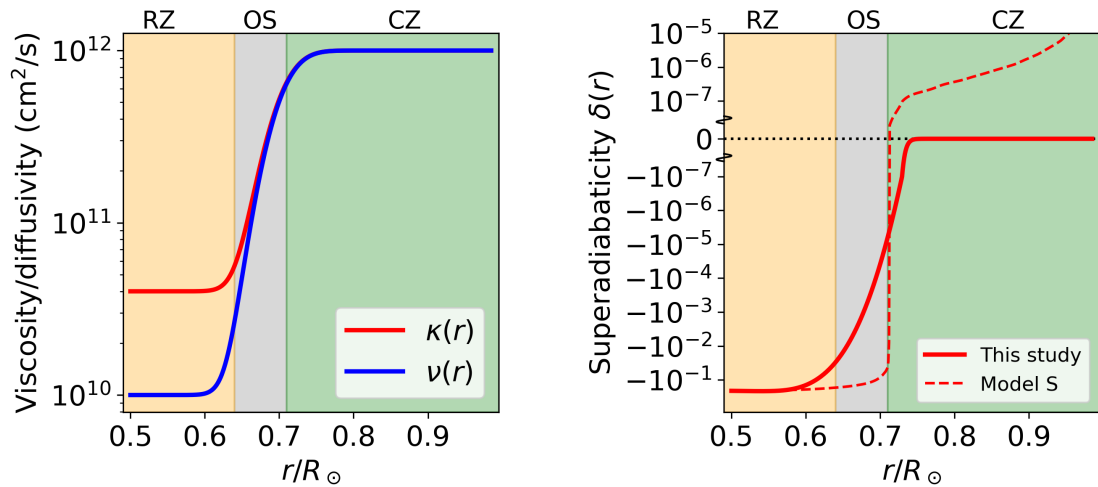


Fig. 2. Left: Profiles of turbulent viscosity $\nu(r)$ and turbulent thermal diffusivity $\kappa(r)$ as functions of radius. They are expressed by Eqs. (8) and (9). Right: Profile of superadiabaticity $\delta(r)$ as a function of radius (Eq. 10). The superadiabaticity profile from the standard model S is represented by the red dashed curve (Christensen-Dalsgaard et al. 1996). The y-axis is linear for $|\delta| < 10^{-7}$ and logarithmic beyond that. In both panels, the green shaded area denotes the convection zone, the grey shaded region denotes the overshooting layer, and the orange shaded region denotes the radiative zone.

which smoothly connects the strongly subadiabatic RZ and the adiabatic bulk CZ,

$$\frac{\partial s_0}{\partial r} = \frac{1}{4} \left(\frac{\partial s_0}{\partial r} \right)_{RZ} \left[1 - \text{erf} \left(\frac{r - r_{\delta 1}}{d_\delta} \right) \right] \left[1 - \text{erf} \left(\frac{r - r_{\delta 2}}{d_\delta} \right) \right], \quad (10)$$

where $r_{\delta 1} = 0.61R_\odot$, $r_{\delta 2} = 0.68R_\odot$, $d_\delta = 0.04R_\odot$, and $(\partial s_0 / \partial r)_{RZ} = 1.32 \times 10^{-2} \text{ erg g}^{-1} \text{K}^{-1} \text{cm}^{-1}$. The right panel of Fig. 2 shows the corresponding radial profile of superadiabaticity $\delta = H_p C_p^{-1} (\partial s_0 / \partial r)$ used in our computations. We note that our $\delta(r)$ profile has a smoother transition from the subadiabatic RZ and the adiabatic CZ than that of model S. This is required in our model in order to avoid oscillations in the projection of the profile onto the Chebyshev basis.

Based on the profiles of turbulent diffusivities and superadiabaticity shown in Fig. 2, our numerical domain can be divided into the following three regions;

- the RZ ($r < 0.64R_\odot$) where turbulent motions are suppressed (ν and κ are substantially small) and the stratification is strongly subadiabatic ($\delta \sim -0.1$),
- the overshooting (OS) layer ($0.64R_\odot \leq r \leq 0.71R_\odot$) where turbulent motions penetrate but the stratification is significantly subadiabatic (e.g. Hotta 2017; Käpylä et al. 2017),
- the CZ ($r > 0.71R_\odot$) where the vigorous convective motions lead to significant values of ν and κ and the stratification is close to adiabatic ($|\delta| \lesssim 10^{-6}$).

These three regions are highlighted by different colours in Fig. 2. Fig. 1c demonstrates that the tachocline with significant radial differential rotation overlaps with the OS defined in our setup.

2.4. Free-surface boundary conditions

We set the lower boundary in the upper RZ at $r_i = 0.5R_\odot$ and the upper boundary slightly below the photosphere at $r_o = 0.985R_\odot$.

At both radial boundaries, in contrast to the conventionally used impenetrable boundary condition, we imposed the free-surface boundary condition for the radial velocity u_r by setting the Lagrangian pressure perturbations to 0. The Lagrangian pressure perturbation, δp , is related to the Eulerian pressure perturbation, p_1 , as

$$\frac{\partial(\delta p)}{\partial t} = \frac{\partial p_1}{\partial t} + \mathbf{u} \cdot \nabla p_0 + \mathbf{v}_0 \cdot \nabla p_1 = 0. \quad (11)$$

Using the wave Ansatz where all the perturbations are assumed to be proportional to $\exp(im\phi - i\omega t)$, this translates to

$$-i\omega p_1 - u_r \rho_0 g + im(\Omega(r, \theta) - \Omega_0) p_1 = 0. \quad (12)$$

The above Eq. (12) was forced at both radial boundaries. We validated this free-surface boundary condition by reproducing the dispersion relation of the f modes on a spherical surface (e.g. Christensen-Dalsgaard 2002; Antia 1998). For low-frequency inertial modes whose oscillation periods are much longer than those of f modes, the free-surface boundary condition is found to almost reduce to the impenetrability condition (e.g. Hindman & Jain 2022, 2023). Nevertheless, the free-surface boundary condition is expected to work better for g modes and gravito-inertial modes in the RZ. In addition, we also apply the conventional horizontal stress-free condition, i.e. $S_{r\theta} = S_{r\phi} = 0$ at both radial boundaries. We assumed that the flux of entropy perturbations vanishes at the bottom boundary, and entropy perturbations vanish at the top boundary.

2.5. Eigenvalue solver

We followed the same approach as Mukhopadhyay et al. (2025) to solve the eigenvalue problem of the governing equations (Eqs. 1–4) with the boundary conditions (Sect. 2.4), considering the wave Ansatz $\exp(im\phi - i\omega t)$ for each azimuthal order m . We solved the sparse problem on the spherical shell basis of Dedalus and selected the modes of interest, in the same way as Mukhopadhyay et al. (2025). We use a typical resolution of 180 points in radius and 60 points in latitude in calculations with the simplified differential rotation. When the observed solar differential rotation is adopted, we use a grid with 90 points in radius and 36 points in latitude. All eigenmodes are converged well below the observational resolutions (Gizon et al. 2021).

3. Inertial modes of the extended model

3.1. Modes confined primarily to the CZ

First, we examine how the inertial modes of the CZ are affected by the presence of RZ below. To this end, we carried out calculations with and without RZ and compared the resultant eigenmodes. The model without RZ has the lower boundary at $r_i = 0.71 R_\odot$ with an impenetrable boundary condition, thereby excluding both OS and RZ. This CZ-only model has been traditionally employed in previous studies (Bekki et al. 2022b; Mukhopadhyay et al. 2025). Except for this lower boundary treatment, the two models are identical.

Figures 3a and b compare the eigenfunctions of the $m = 1$ high-latitude mode, $m = 3$ equatorial Rossby modes with no radial node ($n_{\text{CZ}} = 0$) and with one radial node in CZ ($n_{\text{CZ}} = 1$), the $m = 10$ HFR mode, and the $m = 3$ prograde columnar mode. All of these modes have already been discussed in Mukhopadhyay et al. (2025) within the CZ-only framework. We find that the inclusion of RZ has a limited impact on the eigenfunctions of these

inertial modes within the CZ. In fact, these modes are found to become decaying in the RZ (Fig. 3b). Figure 3c compares the surface velocity eigenfunctions between the two models, where the eigenfunctions are normalized such that the modes have the same total horizontal velocity power at the surface in both models. The differences in the velocity eigenfunctions at the surface ($r = r_o$) can be measured by correlation coefficient

$$C = \frac{\int_S (u_{\theta, \text{RZ}} u_{\theta, \text{CZ}} + u_{\phi, \text{RZ}} u_{\phi, \text{CZ}}) dS}{\sqrt{\int_S (u_{\theta, \text{RZ}}^2 + u_{\phi, \text{RZ}}^2) dS} \sqrt{\int_S (u_{\theta, \text{CZ}}^2 + u_{\phi, \text{CZ}}^2) dS}}, \quad (13)$$

where S represents the spherical surface and \mathbf{u}_{RZ} and \mathbf{u}_{CZ} are from the models with and without RZ, respectively. We find that $C \gtrsim 0.9$ for the inertial modes discussed here, demonstrating that the way these inertial modes are observed at the top of CZ is almost unaffected by the inclusion of RZ. Figure 3d compares the radial variations of the mode power measured by the root-mean-square (RMS) velocity u_{RMS} . It is shown that the power distribution in the bulk CZ is only marginally affected by the inclusion of RZ, except near the base of the CZ, where the deviation can become significant (e.g. $m = 1$ high-latitude mode). Although the modes become decaying in the RZ, they can have finite motions in the OS. This can affect the mode frequencies and growth rates due to its effects on mode dissipation (see Appendix A).

Figure 4 compares the frequencies and growth rates of the above-discussed inertial modes in the two setups. Their mode frequencies are affected by at most a few nHz (< 10 nHz) for most inertial modes except some non-toroidal modes (HFR modes at $m \geq 12$ and prograde columnar modes at $m \leq 6$). The differences in frequencies are remarkably large (> 20 nHz) only for HFR modes at $m > 12$. We note that these HFR modes are special in several aspects: they are strongly non-toroidal and the radial motions tend to be more localized near the base of the CZ as m increases (Bekki 2024). Furthermore, they have the critical latitudes penetrating into the OS (see Fig. 3b). These various factors change the effective rotation rate associated with the mode and cause the apparent shift in the frequency measured in the Carrington frame (refer to Appendix B for details). This Doppler shift of the frequency in the Carrington frame is further amplified for high m . As opposed to Hindman & Jain (2023), the dispersion relation of the prograde columnar modes in our setup is not significantly affected by the inclusion of RZ because strongly subadiabatic RZ itself acts like a lower boundary to these convective modes.

Although the changes in the frequencies are rather insignificant for most inertial modes, the inclusion of RZ has a stronger impact on the mode growth rates. As shown in the bottom panel of Fig. 4, the modes tend to be more damped when the RZ is included. Figure A.1 demonstrates the dissipation in OS caused by the inclusion of RZ. For high m , the modes tend to be restricted to the outer part of CZ, causing their growth rates to be not significantly affected by the inclusion of RZ. This cannot be seen for the HFR modes because they still exhibit significant motions throughout CZ at $m = 16$, as their critical latitudes are located near the base of CZ.

3.2. Modes confined primarily to the RZ

Next, we discuss the modes that have dominant motions in the RZ. We find that there exist quasi-toroidal inertial modes trapped inside the RZ whose eigenfunctions are well represented by the spherical harmonics and follow the dispersion relations of the

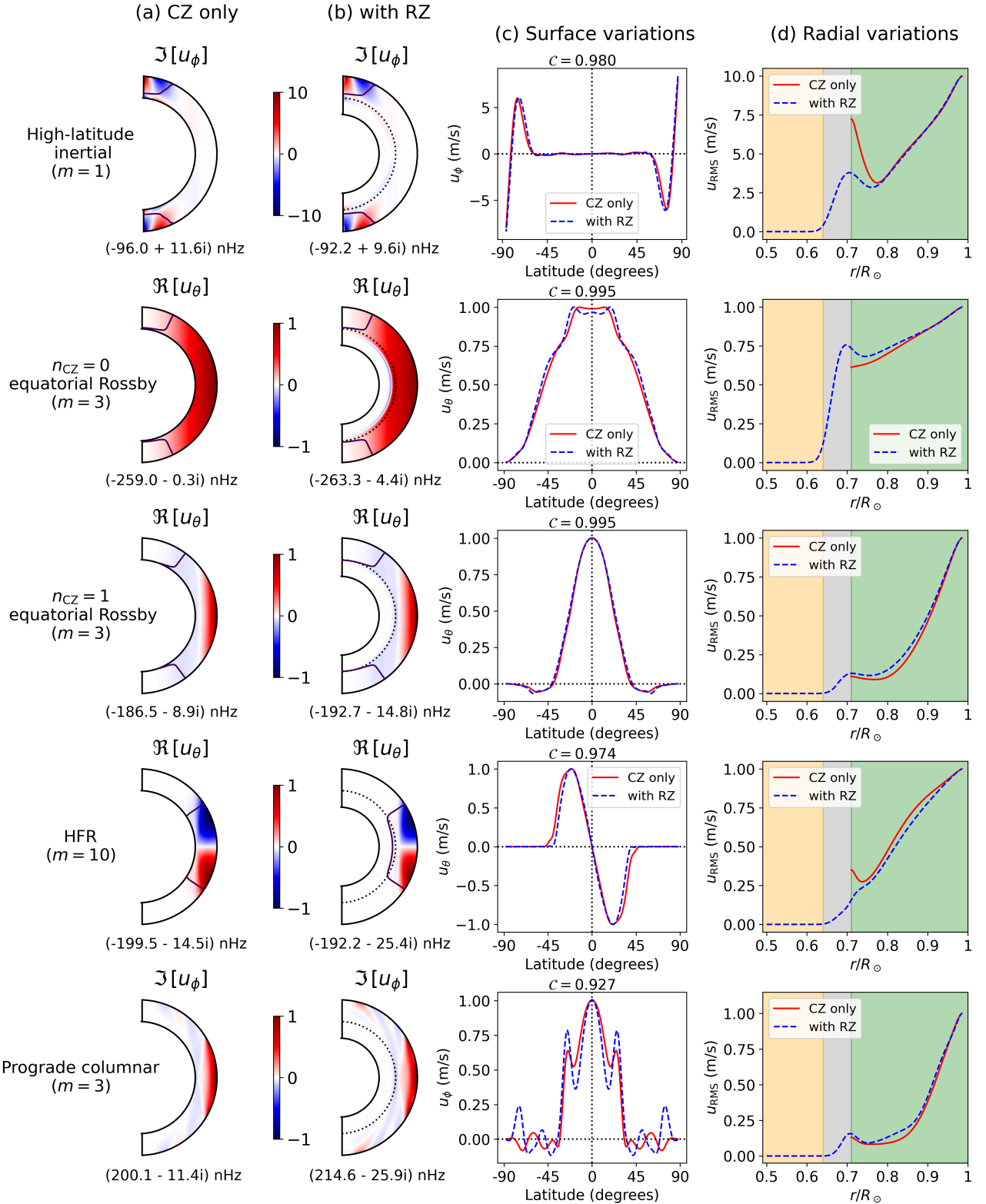


Fig. 3. Comparison of selected inertial modes computed in the setups that include and exclude RZ, respectively. (a) Velocity eigenfunctions in meridional cross-sections from the CZ-only model. The real part of the eigenfunction corresponds to a longitude ϕ_0 (where u_θ is maximum), while the imaginary part corresponds to the longitude $\phi_0 - \pi/2m$. The $m = 1$ high-latitude mode is normalized to have the maximum surface velocity 10 m s^{-1} , while the others are normalized to have a maximum surface velocity 1 m s^{-1} . Black solid curves denote the critical latitudes of the mode where $\Re[\omega] = m(\Omega - \Omega_0)$. The frequencies are measured in the Carrington frame. (b) Same as panel (a) but from the extended model including RZ. Black dotted lines denote the base of the CZ. (c) Horizontal velocity eigenfunctions as functions of latitude at the surface. Blue dashed and red solid curves represent the results with and without RZ, respectively. The correlation coefficient between the eigenfunctions, C , defined in Eq. (13), is mentioned above each subplot. (d) Radial profiles of the RMS velocity.

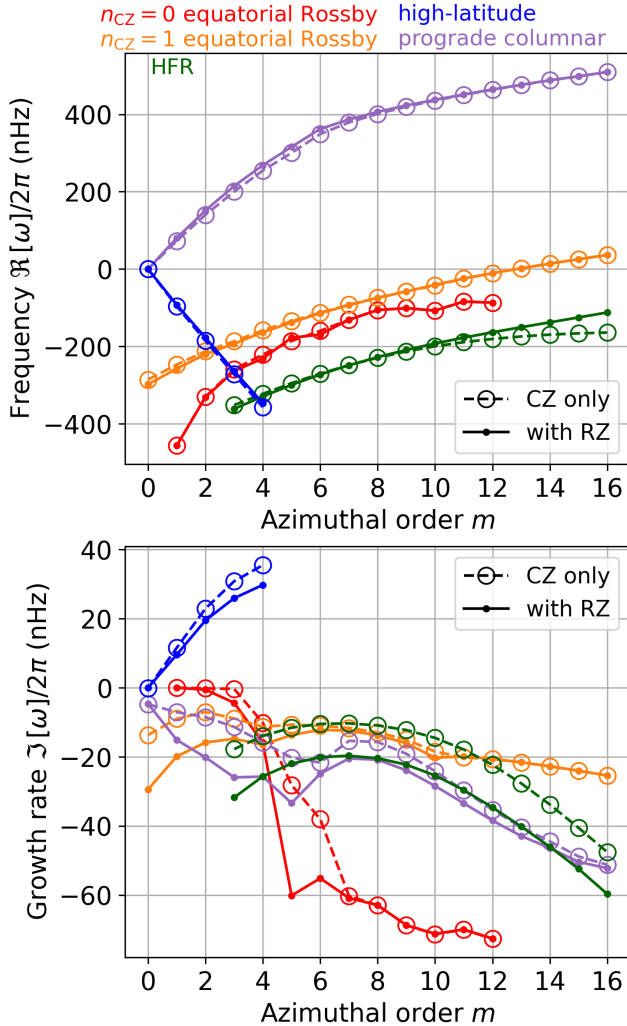


Fig. 4. Top: Dispersion relations of the inertial modes in CZ computed in the setups including RZ (solid lines with points) and excluding RZ (dashed lines with open circles). The colours denote the various types of inertial modes. Bottom: Growth rates of the same modes, with the same notations.

classical Rossby modes

$$\omega_{\ell,m}^R = -\frac{2m\Omega_{RZ}}{\ell(\ell+1)} + m(\Omega_{RZ} - \Omega_0), \quad (14)$$

where ℓ is the harmonic degree. Here, the second term represents the Doppler frequency shift in the Carrington frame. For each combination of (ℓ, m) , these RZ Rossby modes can have any number of radial nodes n_{RZ} at the same frequencies $\omega_{\ell,m}^R$, where n_{RZ} is counted for u_θ in the region $0.5R_\odot \leq r \leq 0.71R_\odot$. Figure 5 displays their dispersion relations for $\ell - m = 0, 1$, and 2 , with two different n_{RZ} , clearly demonstrating that the computed frequencies agree strikingly well with the theoretical prediction (Eq. 14) and that the frequencies are independent of n_{RZ} .

Figure 6a shows the complex eigenfrequency spectrum at $\ell = m = 3$. The equatorial Rossby mode inside the CZ discussed in Sect. 3.1 can be identified at $\Re[\omega]/2\pi = -263.3$ nHz (denoted by the cross symbol). Apart from that, near the classical Rossby mode frequency $\omega_{\ell=m=3}^R$, there exist many RZ Rossby modes with different n_{RZ} (denoted by star symbols). Their growth rates decrease with the increase of n_{RZ} as dissipation increases with n_{RZ} (see Appendix A). Figures 6b and c further show the merid-

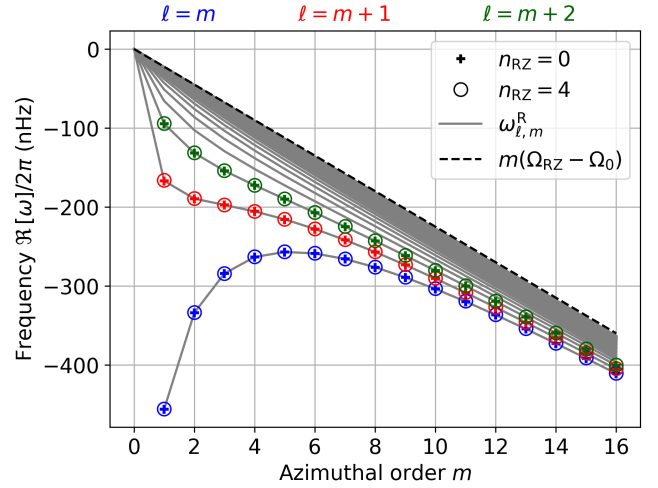


Fig. 5. Dispersion relations of the Rossby modes inside the RZ with $\ell = m$ (navy blue), $\ell = m + 1$ (red), $\ell = m + 2$ (dark green) for azimuthal orders $1 \leq m \leq 16$. The frequencies are measured in the Carrington frame. The plus symbols ($n_{RZ} = 0$) and open circles ($n_{RZ} = 4$) denote modes with different number of radial nodes n_{RZ} in the region $0.5R_\odot \leq r \leq 0.71R_\odot$. The grey solid curves represent the theoretical dispersion relations of the classical Rossby modes $\omega_{\ell,m}^R$ given by Eq. (14). The dashed black line denotes the maximum possible value of $\omega_{\ell,m}^R$.

ional eigenfunctions of the RZ Rossby modes at $n_{RZ} = 0$ and 3 , respectively. It is clearly seen that the modes are strongly confined inside the RZ and become decaying in the CZ. Since the RZ is uniformly rotating and no critical latitudes exist, the horizontal eigenfunctions in the RZ show no major deviations from the corresponding spherical harmonics. We also note that these RZ Rossby modes have substantial entropy perturbations arising from the strongly subadiabatic background stratification.

As has been reported in Blume et al. (2024), the Rossby modes in the subadiabatic RZ can have any allowed combination of (ℓ, m) , including the non-sectoral ($\ell \neq m$) components (see also Fig. 5). This is in striking contrast to the Rossby modes in the adiabatically stratified CZ, where only sectoral ($\ell = m$) modes can exist, as only sectoral modes can sustain the required radial force balance between the Coriolis and pressure gradient forces (Provost et al. 1981; Damiani et al. 2020). In the subadiabatic RZ, on the other hand, the radial component of the Coriolis force can be balanced by the combined effect of buoyancy and pressure to maintain the toroidal nature of these Rossby modes. To confirm this, we analyse the force balance in the RZ Rossby modes. The various forces are given by

$$\mathbf{F}_{\text{Coriolis}} = -2\Omega_0(\mathbf{e}_z \times \mathbf{u}), \quad (15)$$

$$\mathbf{F}_{\text{Pressure}} = -\nabla\left(\frac{p_1}{\rho_0}\right), \quad (16)$$

$$\mathbf{F}_{\text{Buoyancy}} = \frac{s_1}{c_p} g \mathbf{e}_r, \quad (17)$$

$$\mathbf{F}_{\text{Viscous}} = \frac{1}{\rho_0} \nabla \cdot (\nu \rho_0 \mathbf{S}). \quad (18)$$

Figure 7 presents the analysis for a non-sectoral RZ Rossby mode with $(\ell, m) = (4, 3)$. Figure 7a shows that the mode is quasi-toroidal, where the radial motions are several orders of magnitude smaller than the horizontal motions. However, the small radial motions induce a substantial buoyancy force in the subadiabatic RZ to balance the radial pressure gradient and Coriolis forces (Fig. 7b). Nevertheless, the geostrophic nature of the

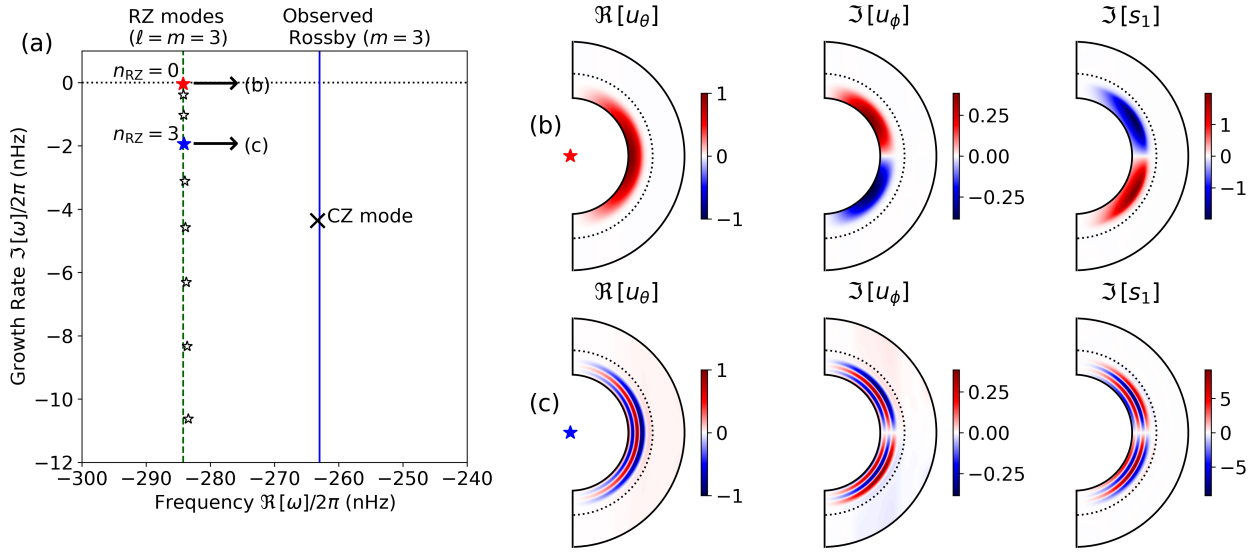


Fig. 6. Position of the RZ Rossby modes with $\ell = m = 3$ in the complex frequency space and their eigenfunctions. (a, left) Complex frequency spectrum of equatorial Rossby modes in the radiative interior with azimuthal order $m = 3$. Star symbols denote the RZ Rossby modes, while the cross symbol denotes the CZ Rossby mode. Red and blue stars denote the RZ Rossby modes with number of nodes in the region $0.5R_\odot \leq r \leq 0.71R_\odot$, $n_{RZ} = 0$ and $n_{RZ} = 3$, respectively. The vertical solid blue line denotes the observed Rossby mode frequency, while the vertical dashed green line denotes the frequency given by Eq. (14). (b) Meridional eigenfunction of the RZ Rossby mode with $n_{RZ} = 0$ (red star). The real and imaginary components denote longitudes in the same way as Fig. 3. The dotted lines denote the position of the base of CZ. The eigenfunctions are normalized such that the maximum of u_θ is 1 m s^{-1} . The unit of s_1 is $\text{erg g}^{-1} \text{ K}^{-1}$. (c) Same as (b) but for the RZ Rossby mode with $n_{RZ} = 3$ (blue star).

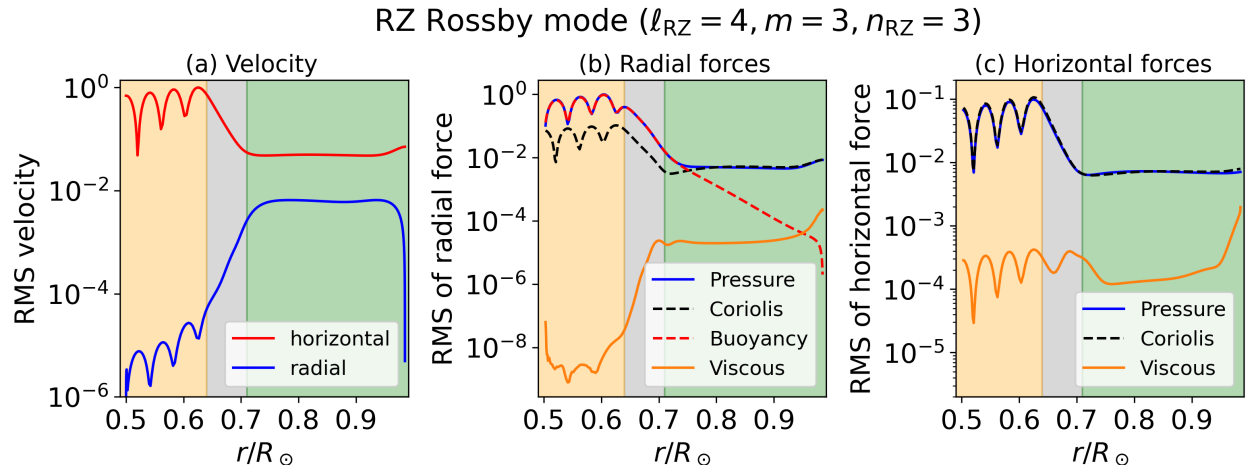


Fig. 7. Analyses of the non-sectoral Rossby mode in the RZ with $\ell_{RZ} = 4$, $m = 3$, $n_{RZ} = 3$. (a) Radial profiles of the RMS velocity in the horizontal (red) and radial (blue) directions. The profiles are normalized to have a maximum total RMS velocity of unity. (b) RMS of the radial component of various forces, defined in Eqs. (15) – (18). The pressure gradient force (blue solid), Coriolis force (black dashed), buoyancy force (red dashed), and viscous force (orange solid) are normalized so that the maximum of the pressure gradient force is unity. The colours of the shaded regions have the same notation as in Fig. 2. (c) Same as (b) but for the horizontal component of the forces.

traditional Rossby modes persists in the horizontal force balance (Fig. 7c). This causes the Rossby modes in RZ to have frequencies determined entirely by the rotation rate, given by Eq. (14).

3.3. CZ-RZ mixed modes

We now explore modes that have significant motions in both the CZ and RZ. In practice, we find that significant mode mixing only occurs when $|\Delta\omega| \lesssim 10 \text{ nHz}$, where $|\Delta\omega|$ is the separation between the RZ Rossby mode and the nearest CZ inertial mode, consistent with avoided-crossing behaviour. Such mode-mixing can occur only when the RZ Rossby mode and its nearest

CZ inertial mode have the same north-south symmetry. In such special cases, we encounter CZ-RZ mixed modes, whose eigenfunctions have substantial amplitudes in both the CZ and RZ. A caveat should be noted: Although we refer to them as mixed modes, they are still essentially RZ Rossby modes that have non-negligible amplitudes in the CZ, and only a subset of RZ Rossby modes are allowed to behave in this way. Figure 8 highlights 11 such examples illustrating how such mode mixing between the RZ and CZ can occur in the dispersion diagrams for both equatorially symmetric and antisymmetric modes. We note that the possible options of mode mixing are quite limited, as the frequencies of the RZ Rossby modes are restricted to a finite range by

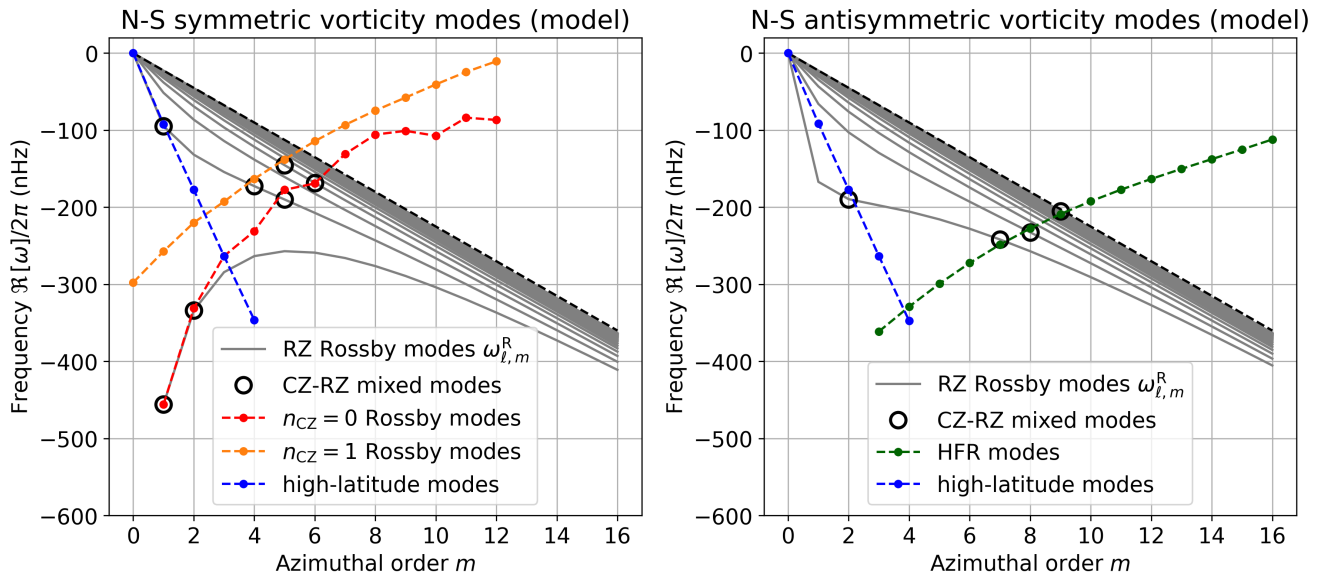


Fig. 8. Frequencies of the retrograde-propagating inertial modes in the CZ (coloured dashed; the same as in Fig. 4) overplotted with the dispersion relations of the RZ Rossby modes (grey solid; given by Eq. (14)). The left and right panels correspond to the modes with north-south symmetric and antisymmetric vorticity, respectively. Open circles denote the RZ Rossby modes, which can form mixed modes with the CZ inertial modes.

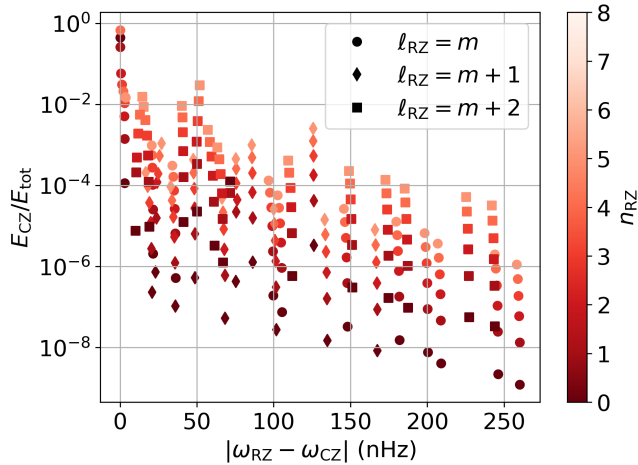


Fig. 9. Fraction of kinetic energy density $E = \langle \rho_0 u^2 \rangle$ of the RZ Rossby modes present in the CZ as a function of the absolute difference of its eigenfrequency and the eigenfrequency of the nearest CZ inertial mode as seen from Fig. 8. We limit to the RZ Rossby modes with $\ell_{RZ} = m$ (circles), $\ell_{RZ} = m + 1$ (diamonds), and $\ell_{RZ} = m + 2$ (squares) for simplicity. The colour of the symbols denotes the number of radial nodes n_{RZ} in the region $0.5R_\odot \leq r \leq 0.71R_\odot$. We only plot the modes with $n_{RZ} \leq 5$ for simplicity.

Eq. (14). For instance, the mixing between the $\ell_{RZ} = m$ Rossby in the RZ and the $n_{CZ} = 0$ equatorial Rossby in the CZ can only occur at $m = 1$ and 2 . Here, ℓ_{RZ} denotes the harmonic degree of the RZ Rossby component of these mixed modes. The $n_{CZ} = 0$ Rossby modes in CZ with $m = 5$ and 6 can also couple with the RZ Rossby modes but with $\ell_{RZ} - m = 2$ and 6 , respectively. A similar coupling is allowed for the $n_{CZ} = 1$ Rossby modes in CZ with $m = 4$ and 5 . As for the high-latitude modes, only the $m = 1$ mode with north-south symmetric vorticity and the $m = 2$ mode with the opposite symmetry can couple with the RZ Rossby modes. Finally, the HFR modes with $m = 7, 8$, and 9 are allowed to couple with the RZ Rossby modes with north-south antisymmetric vorticity. The mode masses of all these mixed modes are,

however, dominated in the RZ (as quantified in Appendix C). We note that there is no mixed mode between the retrograde-propagating RZ Rossby and the prograde-propagating columnar convective modes.

In principle, CZ-RZ mixed modes are allowed to have any number of radial nodes n_{RZ} in the region $0.5R_\odot \leq r \leq 0.71R_\odot$, since the frequencies of the RZ Rossby modes are independent of n_{RZ} . However, n_{RZ} has a significant impact on how the mode power is distributed between the CZ and RZ: As n_{RZ} increases, the relative velocity amplitude in the CZ increases. A possible explanation for this is given in Appendix A. Figure 9 displays the normalized kinetic energy within the CZ of the RZ Rossby modes as a function of the absolute frequency difference $|\Delta\omega|$ from the nearest CZ inertial modes. It clearly shows that the mode tends to be more strongly coupled and has more power inside the CZ when $|\Delta\omega|$ is smaller. It is also demonstrated that the fraction of kinetic energy in the CZ increases with n_{RZ} . These results collectively indicate that, for an RZ Rossby mode to be a CZ-RZ mixed mode, it must have high n_{RZ} as well as a frequency sufficiently close ($|\Delta\omega| \lesssim 10$ nHz) to that of the corresponding CZ inertial mode.

The velocity eigenfunctions of the selected CZ-RZ mixed modes are compared in Fig. 10 with those of the CZ inertial modes (discussed in Sect. 3.1), showing overall remarkable similarity in CZ. Notably, the surface eigenfunctions exhibit only minor differences, suggesting that it is challenging to determine from surface observations alone whether the mode is mixed with the RZ Rossby modes or not.

4. Discussion

4.1. Most CZ modes are weakly affected by the RZ

In this work, we extended the linear model of inertial modes in the Sun's differentially rotating CZ of Mukhopadhyay et al. (2025) to include the subadiabatic RZ. To study how the RZ affects the solar inertial modes in the CZ, we first compared the eigenmodes computed in models that include and exclude the RZ. We find that the mode frequencies are only marginally af-

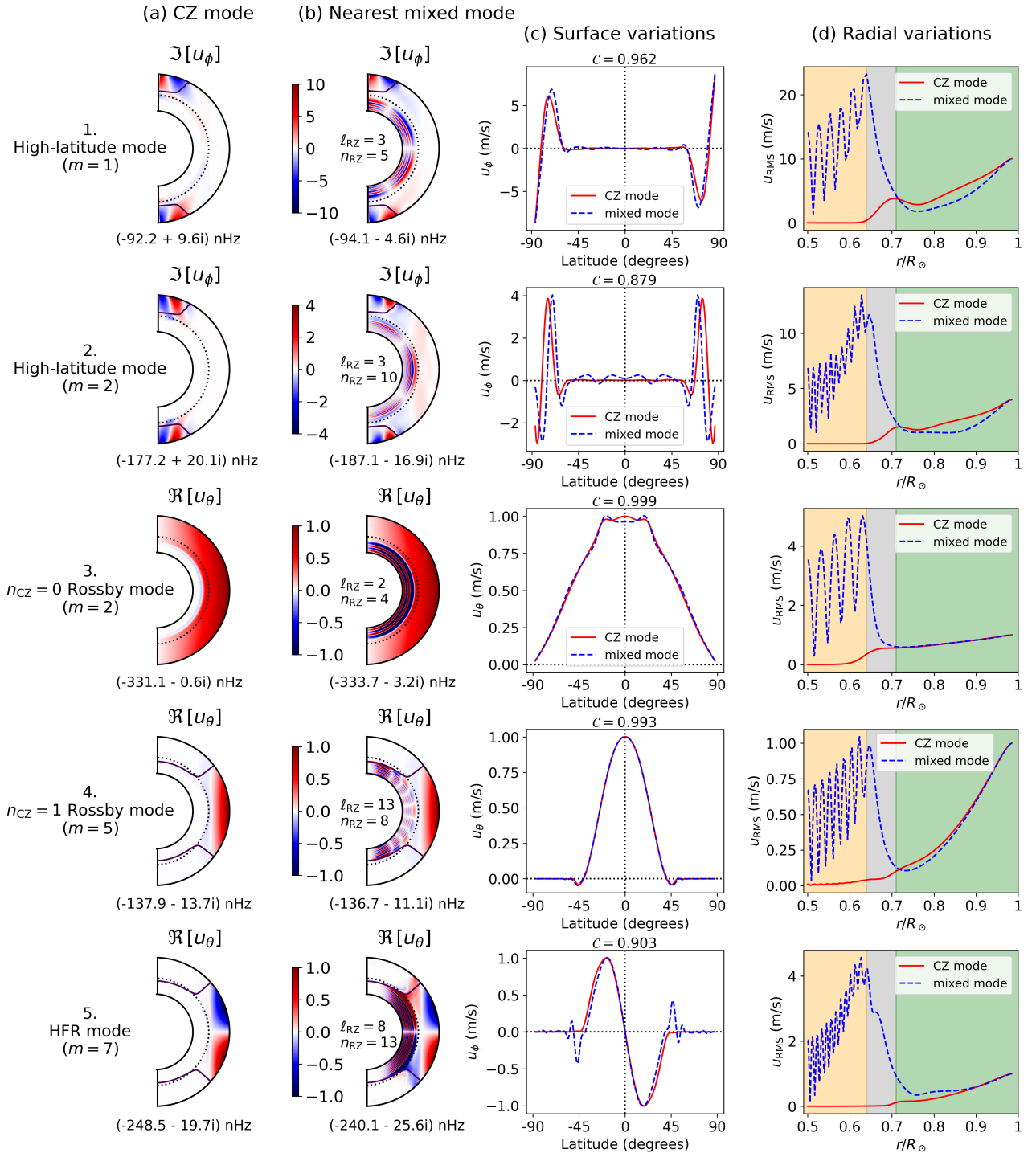


Fig. 10. Selected inertial modes computed in the extended setup, which includes the RZ. (a) modes with motions predominant in CZ and decaying in RZ. (b) modes with comparable motions in RZ and CZ, with flows in CZ similar to the mode in the same row in (a). Surface and radial variations of the modes are represented in (c) and (d), like in Fig. 3. The notations and layout are the same as in Fig. 3. The spherical harmonic degree and number of radial nodes in the region $0.5R_\odot \leq r \leq 0.71R_\odot$ of the RZ Rossby modes are denoted by ℓ_{RZ} and n_{RZ} , respectively. The $m = 1$ high-latitude modes are normalized to have the maximum velocity of 10 m s^{-1} on the surface, the $m = 2$ high-latitude modes are normalized to have the maximum of 4 m s^{-1} on the surface, while the other modes are normalized to have the maximum velocity of 1 m s^{-1} at the surface.

fected (a few nHz) by the inclusion of the RZ, besides some non-toroidal modes (HFR modes at $m \geq 12$ and prograde columnar modes at $m \leq 6$). In the model with the RZ, the eigenfunctions are found to slowly decay in the OS before vanishing in the RZ. The associated viscous dissipation in the OS leads to larger damping rates of these inertial modes. Within the CZ, the eigenfunctions are primarily altered near the base of the CZ.

On the other hand, the surface eigenfunctions are shown to be almost insensitive to the inclusion of the RZ. Therefore, while the RZ introduces only minor modifications, the CZ-only model remains a valid and practical framework for studying the dispersion relations and surface eigenfunctions of the solar inertial modes and for interpreting the solar observations. If very accurate frequencies and eigenfunctions are desired, inclusion of the

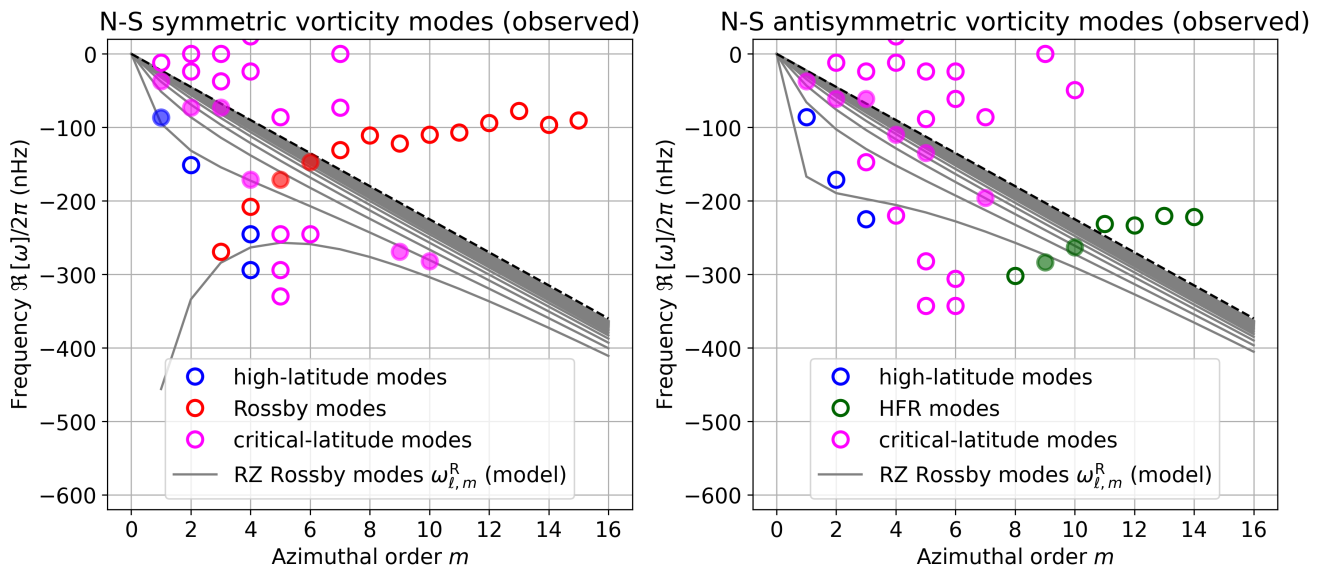


Fig. 11. Frequencies of the observed solar inertial modes (open circles; from Löptien et al. (2018); Gizon et al. (2021); Hanson et al. (2022)) overplotted with the dispersion relations of the RZ Rossby modes (grey solid; given by Eq. 14). The left and right panels correspond to the modes with north-south symmetric and antisymmetric vorticity, respectively. The various observed inertial modes are high-latitude (blue), Rossby (red), HFR (green), and critical-latitude (magenta) modes, which are partially-transparently filled when their frequencies are within 10 nHz of any of the RZ Rossby mode frequencies ($|\Delta\omega| \lesssim 10$ nHz).

Table 1. Mode mass of CZ and mixed modes shown in Fig. 10.

modes from Fig. 10	mode mass ($10^{-3} M_{\odot}$)	frequency (nHz)	mode type (in CZ)
1. (a) CZ	5.9	-92.2	
1. (b) mixed	163.5	-94.1	high-lat. $m = 1$
2. (a) CZ	5.5	-177.2	
2. (b) mixed	317.9	-187.1	high-lat. $m = 2$
3. (a) CZ	16.2	-331.1	
3. (b) mixed	773.7	-333.7	Rossby $m = 2$
4. (a) CZ	2.7	-137.9	
4. (b) mixed	34.9	-136.7	Rossby $m = 5$
5. (a) CZ	2.6	-248.5	
5. (b) mixed	594.4	-240.1	HFR $m = 7$

computational domain until $0.55R_{\odot}$ will suffice as the eigenfunctions vanish by $0.6R_{\odot}$ (see Fig. 3).

4.2. Rossby modes in RZ and their coupling with CZ modes

As found by Blume et al. (2024), the subadiabatic and uniformly rotating RZ can host a wide variety of quasi-toroidal Rossby modes, including the non-sectoral ones (which do not exist in the quasi-adiabatic CZ). We find that they follow the classical Rossby mode dispersion relation (Eq. 14) and have horizontal eigenfunctions well represented by spherical harmonics. They can have all possible combinations of $(\ell_{\text{RZ}}, m, n_{\text{RZ}})$, because the radial force balance can be maintained with the help of buoyancy. As the number of radial nodes n_{RZ} increases, the RZ Rossby modes are more damped, and in turn, have more power in the CZ (see Appendix A). We find that, when the frequencies of the RZ Rossby modes are within ~ 10 nHz of the nearest CZ inertial mode with the same north-south symmetry, these RZ Rossby modes couple with CZ to have substantial eigenfunctions remarkably similar to those of the CZ inertial modes. We referred to such modes as CZ-RZ mixed modes. We note that these

couplings would have been very different if one used uniform rotation throughout the domain, as the frequency of Rossby modes in RZ is entirely determined by the rotation rate in RZ (see Appendix D). Blume et al. (2024) discusses two separate Rossby wave cavities in the stably-stratified RZ and adiabatic CZ. Our studies suggest that the separation of Rossby mode frequencies in CZ and RZ is primarily due to differential rotation. Furthermore, CZ Rossby modes cannot mix with sectoral Rossby modes in RZ for $m > 2$ because of the difference in frequencies, but the RZ Rossby modes can mix with other inertial modes in CZ under the set of concurrent conditions found in our work.

4.3. Detectability of CZ-RZ mixed modes

One may ask if any of the CZ-RZ mixed inertial modes can be observed, as many of these modes have comparable growth rates to the CZ inertial modes (see Fig. 10). The surface eigenfunctions and frequencies of many CZ inertial modes and their nearest CZ-RZ mixed modes are likely too similar to be distinguished using surface observations alone. Figure 11 shows the frequencies of the observed solar inertial modes. Many of the observed modes have frequencies close to those of the RZ Rossby modes, sharing the same north-south symmetry, which enables their coupling with the RZ Rossby modes. It is also plausible that some of the RZ Rossby modes with high n_{RZ} extend to the CZ as critical-latitude modes.

A model for the excitation and damping of these modes would certainly help determine whether some of the mixed modes can reach observable amplitudes. For the linearly stable modes, stochastic excitation by convection is likely the dominant mechanism (Philedit & Gizon 2023). However, as reported in Table 1 (see also Appendix C), the mixed modes are shown to possess a mode mass (see e.g. Christensen-Dalsgaard 2002; Baudin et al. 2005) much higher than those of the CZ inertial modes. This makes it energetically difficult to excite such mixed modes by turbulent convection in the CZ. In the case of linearly unsta-

ble modes, dedicated non-linear simulations will be required to estimate saturation amplitudes reliably (Bekki et al. 2024).

4.4. Implications of horizontal motions below the CZ

We find that the CZ inertial modes have remarkably significant motions in the OS (see Fig. 3). The $m = 1$ high-latitude mode has RMS velocity $\sim 3 \text{ m s}^{-1}$ in the OS, when normalized by the observed amplitude at the surface. The $m = 3$ equatorial Rossby mode also has RMS velocity $\sim 0.7 \text{ m s}^{-1}$ in the OS, while the other modes shown in Fig. 3 have RMS velocities $\lesssim 0.2 \text{ m s}^{-1}$ in the OS. Furthermore, CZ-RZ mixed modes have higher velocities in RZ as compared to CZ because of less dissipation in RZ (refer to Appendix A). The presence of these (mostly horizontal) motions in the subadiabatic OS may contribute significantly to horizontal turbulent diffusion in the solar tachocline (see discussion by Garaud et al. 2025). They could also aid in the confinement of the tachocline through local dynamo effects (e.g. Matilsky et al. 2022).

Acknowledgements. Author contributions: LG and XZ initiated this project, SM implemented all the equations in Dedalus and performed the computations and analysis, YB provided supervision to validate the results, all authors discussed the results, SM wrote the initial draft, and all authors contributed to the final manuscript. We thank P. Dey, D. Fournier, and R. H. Cameron for helpful discussions. SM is a member of the International Max Planck Research School for Solar System Science at the University of Göttingen. YB and LG acknowledge support from ERC Synergy Grant WHOLE SUN 810218. XZ acknowledges the financial support from the German Research Foundation (DFG) through grants 521319293, 540422505, and 550262949.

Matilsky, L. I., Hindman, B. W., Featherstone, N. A., Blume, C. C., & Toomre, J. 2022, *ApJ*, 940, L50
 Mukhopadhyay, S., Bekki, Y., Zhu, X., & Gizon, L. 2025, *A&A*, 696, A160
 Nandy, D. & Choudhuri, A. R. 2002, *Science*, 296, 1671
 Ouazzani, R. M., Lignières, F., Dupret, M. A., et al. 2020, *A&A*, 640, A49
 Pedlosky, J. 1982, *Geophysical fluid dynamics* (Heidelberg: Springer Berlin)
 Philidet, J. & Gizon, L. 2023, *A&A*, 673, A124
 Provost, J., Berthomieu, G., & Rocca, A. 1981, *A&A*, 94, 126
 Samadi, R., Goupil, M.-J., & Lebreton, Y. 2001, *A&A*, 370, 147
 Thompson, M. J., Christensen-Dalsgaard, J., Miesch, M. S., & Toomre, J. 2003, *ARA&A*, 41, 599
 Tokuno, T. & Takata, M. 2022, *MNRAS*, 514, 4140
 Unno, W., Osaki, Y., Ando, H., & Shibahashi, H. 1979, *Nonradial oscillations of stars* (Tokyo: University of Tokyo Press)
 Vasil, G. M., Lecoanet, D., Brown, B. P., Wood, T. S., & Zweibel, E. G. 2013, *ApJ*, 773, 169

References

Alvan, L., Brun, A. S., & Mathis, S. 2014, *A&A*, 565, A42
 Antia, H. M. 1998, *A&A*, 330, 336
 Baudin, F., Samadi, R., Goupil, M.-J., et al. 2005, *A&A*, 433, 349
 Bekki, Y. 2024, *A&A*, 682, A39
 Bekki, Y., Cameron, R. H., & Gizon, L. 2022a, *A&A*, 666, A135
 Bekki, Y., Cameron, R. H., & Gizon, L. 2022b, *A&A*, 662, A16
 Bekki, Y., Cameron, R. H., & Gizon, L. 2024, *Science Advances*, 10, eadk5643
 Bhattacharya, J. & Hanasoge, S. M. 2023, *ApJS*, 264, 21
 Blume, C. C., Hindman, B. W., & Matilsky, L. I. 2024, *ApJ*, 966, 29
 Brown, B. P., Vasil, G. M., & Zweibel, E. G. 2012, *ApJ*, 756, 109
 Brun, A. S., Miesch, M. S., & Toomre, J. 2011, *ApJ*, 742, 79
 Burns, K. J., Vasil, G. M., Oishi, J. S., Lecoanet, D., & Brown, B. P. 2020, *Physical Review Research*, 2, 023068
 Christensen-Dalsgaard, J. 2002, *Reviews of Modern Physics*, 74, 1073
 Christensen-Dalsgaard, J., Dappen, W., Ajukov, S. V., et al. 1996, *Science*, 272, 1286
 Damiani, C., Cameron, R. H., Birch, A. C., & Gizon, L. 2020, *A&A*, 637, A65
 Dintrans, B. & Rieutord, M. 2000, *A&A*, 354, 86
 Fournier, D., Gizon, L., & Hyest, L. 2022, *A&A*, 664, A6
 Garaud, P., Gough, D. O., & Matilsky, L. I. 2025, *ApJ*, 985, 151
 Gizon, L., Bekki, Y., Birch, A. C., et al. 2024, in *IAU Symposium*, Vol. 365, *Dynamics of Solar and Stellar Convection Zones and Atmospheres*, ed. A. V. Getling & L. L. Kitchatinov, 207–221
 Gizon, L., Cameron, R. H., Bekki, Y., et al. 2021, *A&A*, 652, L6
 Gizon, L., Fournier, D., & Albekioni, M. 2020, *A&A*, 642, A178
 Greenspan, H. P. 1968, *The theory of rotating fluids* (Cambridge: Cambridge University Press)
 Hanson, C. S. & Hanasoge, S. 2024, *Physics of Fluids*, 36, 086626
 Hanson, C. S., Hanasoge, S., & Sreenivasan, K. R. 2022, *Nature Astronomy*, 6, 708
 Hindman, B. W. & Jain, R. 2022, *ApJ*, 932, 68
 Hindman, B. W. & Jain, R. 2023, *ApJ*, 943, 127
 Hindman, B. W. & Julien, K. 2024, *ApJ*, 960, 64
 Hotta, H. 2017, *ApJ*, 843, 52
 Hotta, H., Kusano, K., & Shimada, R. 2022, *ApJ*, 933, 199
 Käpylä, P. J., Rheinhardt, M., Brandenburg, A., et al. 2017, *ApJ*, 845, L23
 Kerswell, R. R. 1993, *Geophysical and Astrophysical Fluid Dynamics*, 71, 105
 Larson, T. P. & Schou, J. 2018, *Sol. Phys.*, 293, 29
 Löptien, B., Gizon, L., Birch, A. C., et al. 2018, *Nature Astronomy*, 2, 568

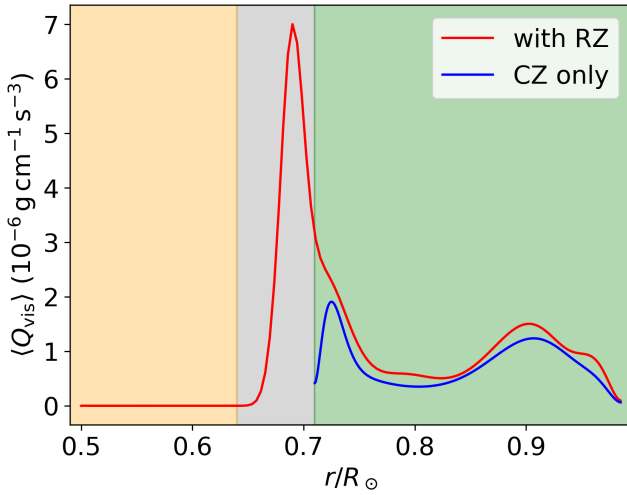


Fig. A.1. Radial profile of dissipation Q_{vis} , defined in Eq. (A.2), for the $m = 3$ prograde columnar mode in the models with (red) and without RZ (blue). The eigenmodes are shown in Fig. 3. They are normalized to have the same total energy density in CZ.

Appendix A: Effects of dissipation in the RZ

In this appendix, we study the effects of dissipation in RZ. For many of the CZ-RZ mixed modes presented in the paper, the velocity amplitude tends to be larger in RZ than in CZ. This Appendix provides a physical reason for this. We also illustrate why the CZ inertial modes are more damped by the inclusion of RZ.

The equation of the kinetic energy density $e_{\text{kin}} = (\rho_0/2)|\mathbf{u}|^2$ can be obtained by taking a dot product of Eq. (1) with \mathbf{u} as

$$\frac{\partial e_{\text{kin}}}{\partial t} = -\nabla \cdot (p_1 \mathbf{u} + \nu \rho_0 \mathbf{u} \cdot \mathbf{S}) - \rho_1 g u_r - Q_{\text{vis}}, \quad (\text{A.1})$$

where Q_{vis} denotes the viscous dissipation of the kinetic energy

$$Q_{\text{vis}} = \frac{\rho_0}{2} \nu \mathbf{S} : \mathbf{S}. \quad (\text{A.2})$$

By taking a volume integral with appropriate radial boundary conditions, we obtain the equation for the total kinetic energy of the toroidal Rossby modes (with $u_r \approx 0$) as

$$\frac{\partial}{\partial t} \int_V e_{\text{kin}} dV = - \int_V Q_{\text{vis}} dV. \quad (\text{A.3})$$

Therefore, the mode damping rate $\gamma = -\Im[\omega]$ can be expressed as

$$2\gamma = \frac{\int_V Q_{\text{vis}} dV}{\int_V e_{\text{kin}} dV}. \quad (\text{A.4})$$

The order of magnitude estimation $\mathbf{S} : \mathbf{S} \approx k^2 |\mathbf{u}|^2$, where k is the local wavenumber, implies that the damping γ goes up with the number of radial nodes.

The mode damping rate is given as the radial average of νk^2 weighted by the kinetic energy density e_{kin} . In general, there is a tendency for eigenmodes to distribute more (less) kinetic energy into a region where the dissipation νk^2 is small (large) in order to minimize the mode damping rate γ . This helps explain the increase in the motions in CZ as the number of nodes in RZ increases (because k is increased). This further causes the modes to be more damped by the increase in the number of radial nodes.

Figures 3 and 4 demonstrate that the CZ inertial modes are significantly damped by the inclusion of RZ. We demonstrate that this is caused by the dissipation resulting from the decay of the modes in OS. Figure A.1 shows the spherically averaged radial profile of dissipation Q_{vis} for the $m = 3$ prograde columnar mode. This is the most affected mode among the CZ inertial modes whose eigenfunctions are presented in Fig. 3. The radial profile of Q_{vis} demonstrates that the dissipation is much higher in OS as compared to the whole of CZ. This is because of the sharp decay of the modes in OS, where the viscosity is finite. This causes significant damping of the CZ inertial modes by the inclusion of RZ.

Appendix B: Analysis of HFR modes

In this Appendix, we analyse the cause of the significant difference in the dispersion relations of the HFR modes at $m \geq 12$ between models that include and exclude RZ, as seen in Fig. 4. Here, we analyse the HFR modes with $10 \leq m \leq 16$, as the dispersion relations diverge starting from $m = 10$, although the differences are small for $m < 12$. The effective rotation rate of the mode can be measured by

$$\Omega_{\text{eff}} = \frac{\int \Omega(r, \theta) e_{\text{kin}} dV}{\int e_{\text{kin}} dV}. \quad (\text{B.1})$$

In the Carrington frame, the change in Ω_{eff} causes a Doppler shift of frequency given by

$$\omega_0 = \omega(\Omega_{\text{eff}}) + m(\Omega_{\text{eff}} - \Omega_0), \quad (\text{B.2})$$

where ω_0 is the frequency in the Carrington frame and $\omega(\Omega_{\text{eff}})$ is that in the frame rotating at Ω_{eff} . At high m , small differences in Ω_{eff} cause a significant difference in ω_0 .

The top panel of Fig. B.1 shows that the effective rotation rates Ω_{eff} of the HFR modes are diverging between models with and without RZ, as m increases. The bottom panel of Fig. B.1 compares the frequencies of the HFR modes in the frame rotating at Ω_{eff} , from Eq. (B.2). It portrays that $\omega(\Omega_{\text{eff}})$ is indeed very similar for the HFR modes in both models. The differences in $\omega(\Omega_{\text{eff}})$ between the two models are of the order of the differences in Ω_{eff} in the two models. Therefore, it is demonstrated that the large deviation in the HFR mode frequencies seen in Fig. 4 is simply caused by the difference in the effective rotation rate $\omega(\Omega_{\text{eff}})$.

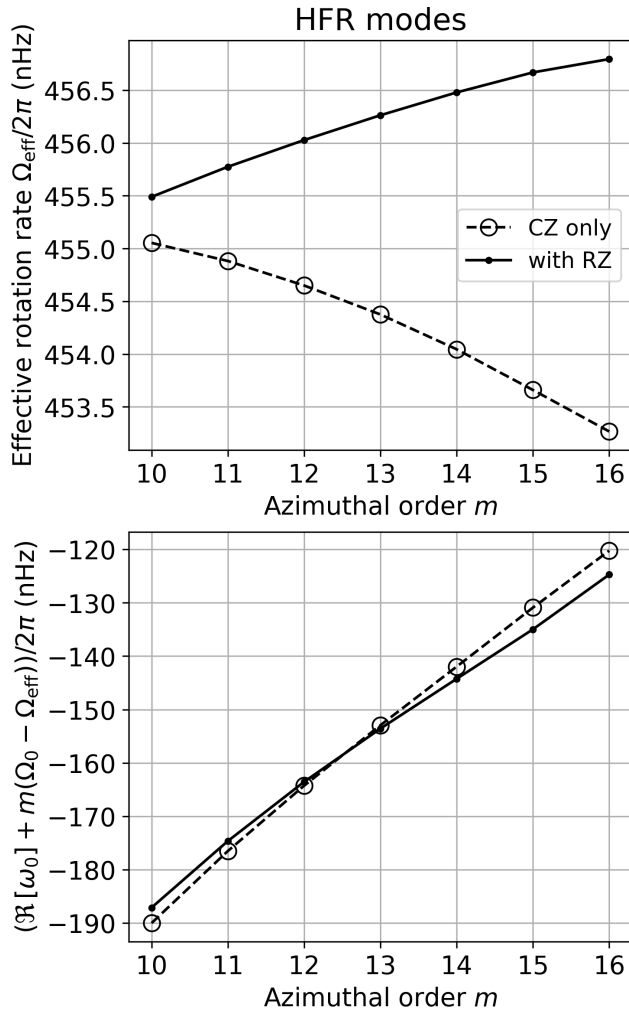


Fig. B.1. *Top:* Effective rotation rate Ω_{eff} , defined in Eq. (B.1), for HFR modes in the models including RZ (solid line with points) and excluding RZ (dashed line with open circles). *Bottom:* Frequency of the modes in the frame rotating at Ω_{eff} , using Eq. (B.2).

Appendix C: Mode mass of the mixed modes

In this Appendix, we report the mode mass of the computed eigenmodes (see e.g. Baudin et al. 2005). The mode mass of an eigenmode is defined as

$$\mathcal{M} = \frac{1}{u_{\text{RMS}}^2(r_s)} \int_V \rho_0 |\mathbf{u}|^2 dV, \quad (\text{C.1})$$

where $u_{\text{RMS}}^2(r_s)$ is the observed mode amplitude at the surface r_s . Note that the mode mass is unaffected by the choice of normalization of the mode. The modes with higher mode mass are more energetically difficult to excite (Samadi et al. 2001).

Figure C.1 presents the mode mass of the CZ-RZ mixed modes and their corresponding CZ inertial modes. It is shown that the mixed modes possess higher mode mass compared to the CZ inertial modes, and the mode mass tends to decrease with increasing n_{RZ} . We note that, due to the very large velocity amplitudes in the RZ, the mode masses of some mixed modes can exceed the solar mass M_{\odot} by several orders of magnitude. These modes are very unlikely to be excited stochastically by turbulent convection in the CZ. Only mixed modes with large enough n_{RZ} could have mode mass close to the CZ inertial modes. On the other hand, our study also reveals that the growth rate of the

mixed modes decreases with an increase in the number of n_{RZ} (see Fig. 6). These competing factors may determine the range of allowed number of radial nodes n_{RZ} of the mixed modes which can be excited to observable amplitudes at the surface.

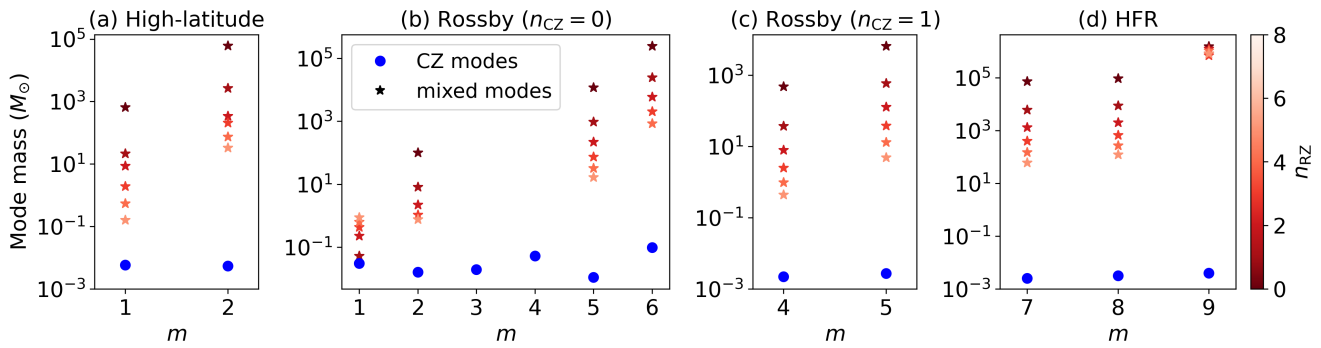


Fig. C.1. Mode mass (Eq. C.1) of the mixed modes (red star) and their nearest inertial mode with motions predominant in CZ (blue dots). The 11 mixed modes marked in Fig. 8 are shown. The colour of the star symbols denotes the number of radial nodes n_{RZ} in the region $0.5R_\odot \leq r \leq 0.71R_\odot$. We only plot the mixed modes with $n_{RZ} \leq 5$ for simplicity.

Appendix D: Case of uniform rotation

In Sect. 3.2, we showed that the Rossby modes in CZ and RZ are separated in frequency due to the presence of differential rotation. This appendix discusses the case of uniform rotation throughout the Sun, $\Omega(r, \theta) = \Omega_0$, while maintaining the radial profiles of all other background quantities. We focus here on the sectoral ($\ell = m$) Rossby modes, because the non-sectoral modes cannot exist in the CZ. Figure D.1 compares the eigenfunctions of the sectoral modes with $1 \leq m \leq 4$ under uniform rotation and those under differential rotation. In the case of uniform rotation, the mode frequencies are given by $\omega_m = -2\Omega_0/(m+1)$ in both CZ and RZ. Therefore, we obtain the eigenmodes that globally span both CZ and RZ. In other words, there is essentially no cavity separating the Rossby modes in the RZ from CZ. We note, however, that the underlying force balance to keep their toroidal nature is different in these two regions: The radial pressure gradient force is balanced by the Coriolis force in the CZ but by buoyancy in the RZ. Consequently, the radial eigenfunctions do not show the well-known r^m dependence (predicted assuming the geostrophic balance) inside the RZ. It is also shown in Fig. D.1 that the mode tends to have a larger velocity amplitude in the RZ than in the CZ as m increases. This is likely because, when the local wavenumber k increases with m , the eigenmode tends to shift more of its power into the less viscous RZ in order to minimize the damping rate (see Appendix A).

In the case of differential rotation in the convection zone, on the other hand, the situation is totally different. The sectoral Rossby modes in the RZ and the equatorial Rossby modes in the CZ (distorted from the original sectoral spherical harmonics by the critical latitudes) have different frequencies, and thus they cannot form a single global eigenmode but instead exist only as isolated, distinct modes. A similar result has been found by Blume et al. (2024), who reported that the CZ and RZ host separate ave cavities for Rossby modes. We note that the only exception is the $\ell = m = 1$ mode, in which the CZ and RZ are strongly coupled. This particular mode, known as a spin-over mode (Kerswell 1993), has a fixed frequency of $-\Omega_0$ and has global motions with quasi-uniform vorticity in a direction perpendicular to the rotational axis (Greenspan 1968). Owing to this special flow structure, this mode is subject to negligible viscous dissipation. Consequently, unlike the other modes discussed above, the spin-over mode does not need to redistribute the power depending on the viscosity, allowing it to have nearly the same eigenfunction both in the CZ and RZ. This mode, however, is difficult to detect because its frequency is (nearly) zero in an inertial frame (-31.7 nHz in the Earth's frame), placing it in a spectral region

often dominated by systematics and signal due to the revolution of the Earth around the Sun.

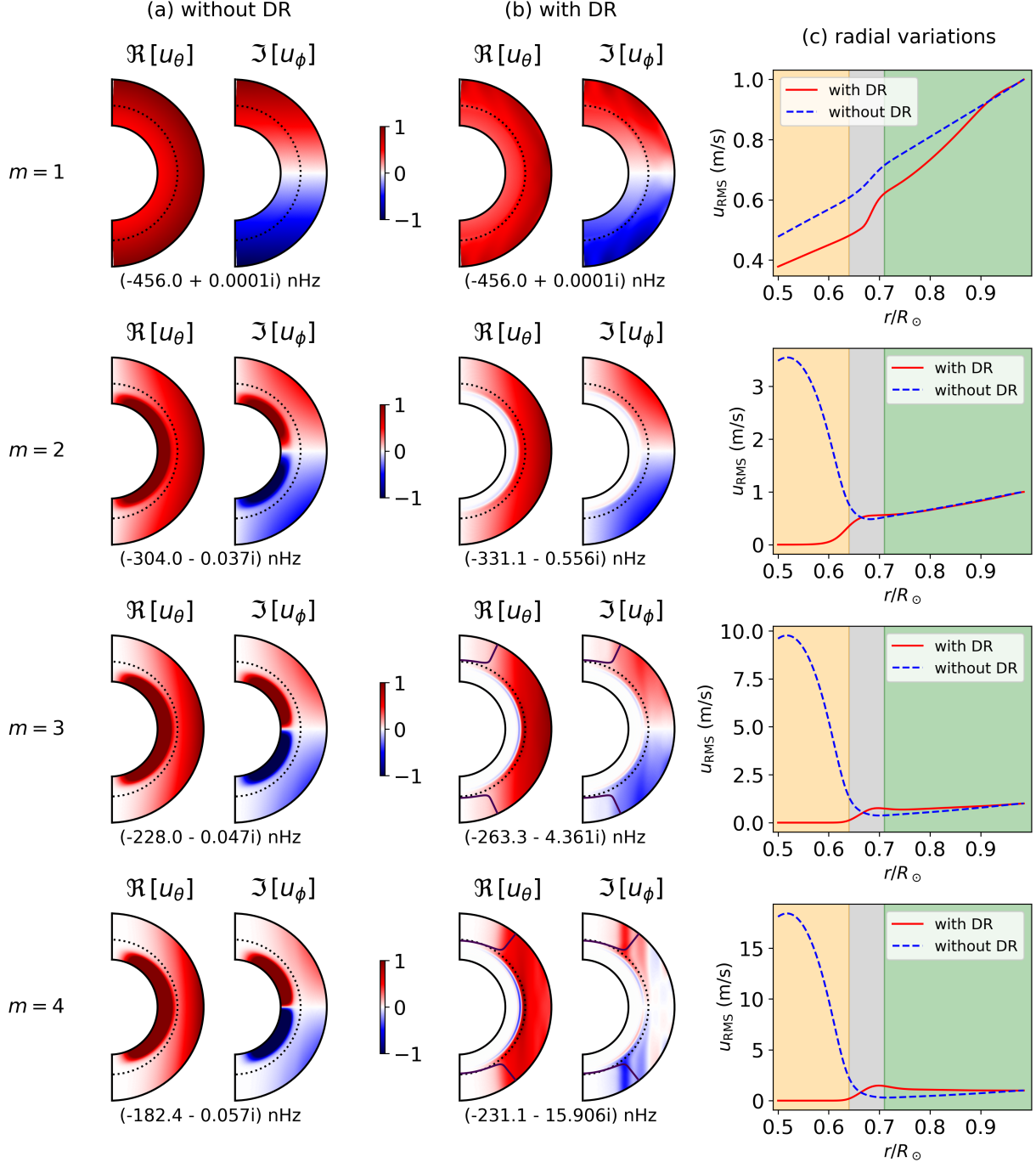
$n_{RZ} = n_{CZ} = 0, \ell_{RZ} = m$ equatorial Rossby modes


Fig. D.1. Analysis of the effects of differential rotation on the sectoral Rossby modes with no nodes in radius ($n_{RZ} = n_{CZ} = 0, \ell_{RZ} = m$). (a) Meridional cross-section of u_θ and u_ϕ of the Rossby modes computed under uniform rotation for different azimuthal orders m . The real and imaginary components denote longitudes in the same way as Fig. 3. The frequencies and the growth rates measured in the Carrington frame are mentioned below the eigenfunctions. All eigenfunctions are normalized to have a maximum of u_θ to be 1 m s^{-1} at the surface. The dotted lines mark the position of the base of CZ. (b) Same as (a), but under simplified differential rotation given by Eq. (5). (c) Comparison of the radial profile of RMS velocity associated with the modes computed with and without differential rotation. The RMS velocity is normalized to be 1 m s^{-1} at the surface. The colours of the shaded regions have the same notation as in Fig. 2.